Deformation microstructures in shock-compressed single crystal and powdered rutile

Yuhei UMEDA[*,**], Yuma NAGAI[**,*], Naotaka TOMIOKA[***,*], Toshimori SEKINE[†], Masashi MIYAKAWA[‡], Takamichi KOBAYASHI[‡], Hitoshi YUSA[‡] and Takuo OKUCHI[*,**]

[*]*Institute for Integrated Radiation and Nuclear Science, Kyoto University, Osaka 590-0494, Japan*
[**]*Graduate School of Engineering, Kyoto University, Kyoto 615-8540, Japan*
[***]*Kochi Institute for Core Sample Research, X-star, Japan Agency for Marine-Earth Science and Technology, Kochi 783-8502, Japan*
[†]*Center for High Pressure Science and Technology Advanced Research, Shanghai 201203, China*
[‡]*Research Center for Materials Nanoarchitectonics, National Institute for Materials Science, Ibaraki 305-0044, Japan*

Shock recovery experiments on the single crystal rutile and the powdered rutile were performed using a single-stage propellant gun to investigate the effects of porosity (i.e., temperature effect) on the formation of shock-induced deformation microstructures. X-ray diffraction and transmission electron microscopy analyses of the shocked single crystal rutile revealed the occurrence of a high-density stacking fault in the {101} plane of rutile. This defect suggests that the dominant slip system causing the plastic deformation of the crystal was $\{101\}\langle\bar{1}01\rangle$ at lower temperatures, forming stacking faults. Additionally, part of the crystal exhibited intergrowth with the α-PbO_2 structure in a topotaxial relationship: $\langle100\rangle_{\mathrm{Rutile}} /\!/ \langle001\rangle_{\alpha\text{-}PbO_2}$. Topological analysis suggests that the single crystal rutile transforms into the α-PbO_2 structure concomitantly with the shear deformation via the fluorite structure. In contrast, the shocked powdered rutile primarily comprises particles with pervasive entangled dislocations and recrystallized particles, where the α-PbO_2 structure was not observed at all. Considering the absence of stacking faults, the dominant slip system in the shocked powdered rutile should have been $\{110\}\langle001\rangle$, which is expected to work more actively at higher temperatures. These contrasting results on shocked rutile indicate that the shock heating effect and the initial porosity significantly influenced the deformation microstructures and high-pressure phase transformations of rutile in shocked meteorites as well as in impact crater rocks.

Keywords: Rutile, Shock recovery experiments, Deformation, Defect structures

INTRODUCTION

The shock response of minerals is essential for understanding the deformation properties of rocks during natural impact events in the histories of the Earth and other planets. Shock compression experiments are the primary methods used to simulate such deformation processes under the known conditions. Microstructural observations of shock-recovered samples have provided valuable indicators for determining the levels of shock pressure and temperature in various types of minerals (Langenhorst, 2002; Fritz et al., 2017; Stöffler et al., 2018). These findings suggested that features of brittle deformation, such as irregular fractures and planar fractures, were dominant under relatively low shock pressures, whereas features of plastic deformation, such as undulatory extinction and mosaicism, were dominant under higher shock pressures (Meyers, 1994; Stöffler et al., 2018). Plastic deformation also produces dislocations, stacking faults, and mechanical twins in shocked minerals, which are identified by transmission electron microscopy (TEM) (Langenhorst, 2002).

We note that shock temperatures differ between reflected shock waves (multiple compressions: conventional shock recovery experiments) and single shock wave (single compression: natural collisions) due to the difference in internal energy increase (Boslough and Asay, 1993). In most cases of shock recovery experiments, the sample is sandwiched between high-impedance metals and subject-

doi:10.2465/jmps.230706
Y. Umeda, umeda.yuhei.2e@kyoto-u.ac.jp Corresponding author

ed to multiple shock compressions generated by the reflection of shock waves between the metals. As a result, the shock pressure and the shock temperature gradually increase (Figs. 16a and 16b in Tomeoka et al., 1999; Fig. 7 in Sharp and DeCarli, 2006). Therefore, when the peak pressure reaches a certain value, the peak shock temperature in multiple shocks is relatively lower than that in a single shock due to the difference in internal energy increase (Tomeoka et al., 1999; Sharp and DeCarli, 2006). In most cases of natural collisions, impactors and targets are subjected to a single shock wave, which has a higher shock temperature than the samples from the shock recovery experiments at the same peak pressure (Wünnemann et al., 2016; Winkler et al., 2018; Kurosawa et al., 2022).

Titanium dioxide (TiO_2) exhibits various crystal structures depending on the pressure and the temperature. Rutile is a stable phase of TiO_2 at the ambient pressure. In nature, the intergrowth of TiO_2 polymorphs has been found in the suevite impactites from the Ries crater in Germany (El Goresy et al., 2001). Therefore, the polymorphism of TiO_2 is an important clue for understanding the pressure and temperature histories of natural impacts (Liou et al., 1998; El Goresy et al., 2001). The α-PbO_2 structure of TiO_2 forms under a wide range of high-pressure conditions, as reported by the static (above ~ 7 GPa) and the dynamic (above ~ 20 GPa) experiments (Kusaba et al., 1988; Nishio-Hamane et al., 2010). In the case of dynamic compression, the phase transition boundary between rutile and the α-PbO_2 structure depends not only on the pressure but also on the crystal orientation to the shock compression axis (Syono et al., 1987; Kusaba et al., 1988). Despite the occurrence of TiO_2 polymorphs in various natural forms, their formation mechanisms, shock temperature profiles, and origin of intergrowth textures under high-pressure conditions remain poorly understood, mostly because of such a complex transition behavior of TiO_2. Furthermore, only a few studies have carefully described shock deformation microstructures of TiO_2 polymorphs. In the previous study on the shock recovery experiment of TiO_2, stacking faults were observed in the shocked single crystal rutile (Kusaba et al., 1988). On the other hand, stacking faults were not observed in the shocked powdered rutile, even at the similar pressures (Tan et al., 2018). Therefore, to understand the variability of microtextural evolution of TiO_2 in the natural impact events, it is very meaningful to compare the textural characteristics of the shock-compressed single crystal and powdered rutile each other, which experience different temperatures at the same peak shock pressure.

This study used a single-stage propellant gun to perform the shock compression experiments on the non-porous (single crystal rutile) and the porous (powdered rutile) samples. The experimental design ensured that these samples experienced the same peak shock pressure. On the other hand, the shock temperature of the powdered rutile was significantly higher than that of the single crystal rutile (Zel'Dovich and Raizer, 2002; Sekine, 2016). This is because the shock compression of the powdered samples involves a large increase in internal energy due to a high degree of the pore collapse and the frictional heating between particle surfaces (Sekine, 2016). Our primary objective was to evaluate potential variations by comparing the deformation microstructure between the shock recovered samples that experienced the different temperatures. For that purpose, a (100) planar single crystal rutile and a powdered rutile were prepared, shock compressed, recovered, and characterized by X-ray diffraction (XRD) and TEM.

EXPERIMENTAL METHODS

Shock recovery experiments

Shock recovery experiments were performed using a single-stage propellant gun at the National Institute for Materials Science, Japan (NIMS). Details of the gun used in this study have been previously described (Sekine, 1997). As shown in Figure 1a, the projectile consists of a steel (SUS304) disk (29 mm in diameter and 3 mm thick) and a sabot (high-density polyethylene) comprising a magnetic disc. The sample container was made of SUS304 (30 mm in diameter and 30 mm in length) with a sample space (18 mm in diameter and 1 mm thick) located 3 mm from the projectile side (Fig. 1a). The samples were sealed with a SUS 304 screw of 25.5 mm length. The projectile was accelerated to the required velocity (1.37 km/s), and the velocity was measured using the magnetic flyer method (Sekine, 1997). The peak shock pressure of 30 GPa was estimated by the impedance mismatch method. Shock recovery experiments were designed to generate the peak pressure of 30 GPa, where the phase transition from rutile to the α-PbO_2 structure was reported to have the highest yield (Kusaba et al., 1988).

The starting material comprised a synthetic single crystal rutile (Crystal Base Co., Ltd., 10 mm × 10 mm × 0.5 mm, purity: 99.99%) or a powdered rutile reagent with a particle size of ~ 2 μm in diameter (Rare Metallic Co., Ltd.). The single crystal was compressed perpendicular to the (100) plane of rutile (Fig. 1b). The experimental setup for compression of this crystal included a free space (thick blue area in Fig. 1b) surrounding the sample in a direction perpendicular to the compression axis. The powdered rutile was annealed at 950 °C for 3 hours to remove the remaining minor anatase. The complete absence of such minor phases was confirmed by powder XRD. The pow-

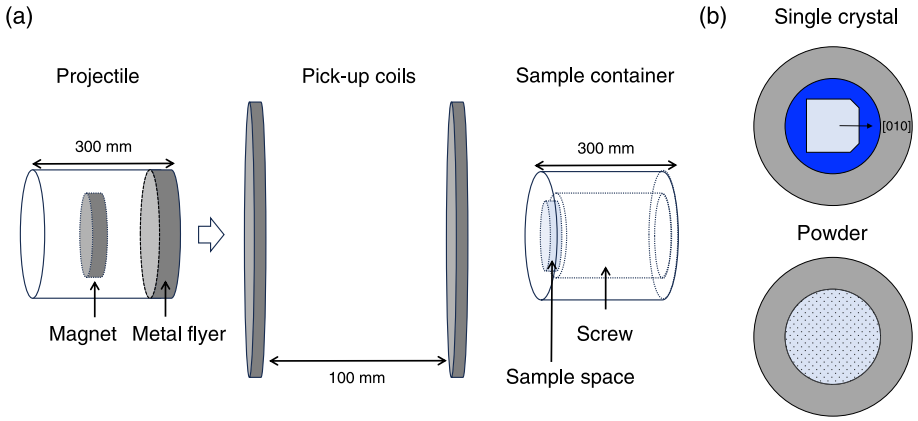

Figure 1. (a) The common setup of shock recovery experiments. (b) The sample setups for the single crystal rutile (top) and the powdered rutile (bottom), with top views of the sample space in the sample container (perpendicular to the collision plane). The samples are shown in light blue.

der pellet of 1.02 ± 0.05 mm in thickness and 17.99 ± 0.05 mm in diameter, measured with a caliper, was prepared using a pelletizer and then placed in the sample container (Fig. 1b). The pellet had a porosity of 28.3 ± 1.5%, which was determined from the volume and weight of the pellet, and the X-ray density of the annealed reagent determined by fitting its XRD pattern. After the shock compression experiments, the shocked samples were recovered from the sample container by cutting a section parallel to the impact plane using a cutting machine (Struers, Accutom-50).

Analytical methods

Part of each recovered sample was ground into fine powder and subjected to XRD analysis for the phase identification, using a Rigaku Ultima IV diffractometer with Cu*K*α radiation driven at 40 mA and 40 kV, which is installed at the Institute for Integrated Radiation and Nuclear Science, Kyoto University (KURNS).

Then, another part of each sample was subjected to TEM and scanning transmission electron microscopy (STEM) analyses. Several 150 nm thick sections for TEM and STEM analysis were prepared using focused ion beam (FIB) instruments FEI Quanta3D200i installed at KRUNS, and HITACHI SMI4050 installed at the Japan Agency for Marine-Earth Science and Technology (JAMSTEC). Following the deposition of the carbon protection layers, the sample surfaces were reduced to ~ 2 µm thick sections and cut using a Ga-ion beam at an accelerating voltage of 30 kV. Subsequently, the sections were mounted on Cu grids using a micromanipulator equipped with FIBs and ultra-thinned. TEM and STEM observations of the ultrathin sections were conducted using a transmission electron microscope (JEOL JEM-ARM200F) at JAMSTEC, operating at an accelerating voltage of 200 kV. Crystallographic and microstructural analyses were performed using selected-area electron diffraction (SAED), bright-field TEM (BF-TEM), and low-angle annular dark-field STEM (LAADF-STEM).

RESULTS

The geometry of the shock-recovered single crystal rutile exhibited ~ 10% length increase along the directions perpendicular to the compression axis. The powder XRD profile of the shocked single crystal rutile showed the coexistence of rutile (Rt) and the α-PbO_2 (α) structures at the peak shock pressure of 30 GPa (Fig. 2a). On the other hand, the shock-recovered powdered rutile became a well-sintered aggregate of submicron-sized particles. The powder XRD profile of the shocked powdered rutile showed only the peaks of rutile even at the same peak shock pressure (Fig. 2b).

Figures 3a and 3b provide an overview of the microtextures of the shocked single crystal rutile observed by TEM. The ultrathin foil sample displayed significant strain contrast and numerous intersecting lineations. The SAED patterns showed the diffraction spots of rutile with streaks along the $<011>^*_{Rt}$ direction (Fig. 3c). These streaks suggest that the lineations are stacking faults lying on two of the four equivalent planes on $\{101\}_{Rt}$. The SAED patterns showed the additional weak spots corresponding to the single crystal of the α-PbO_2 structure. The observed crystallographic relationship between the rutile structure and the α-PbO_2 structure was identified as $<100>_{Rt}$ // $<001>_{\alpha}$. Owing to the complex microstructure with possible overlaps and a high density of stacking faults on the $\{101\}_{Rt}$ planes, the lattice fringes of the α-PbO_2 structure could not be recognized in the high-resolution TEM images.

Figure 4 shows the TEM images of the shocked powdered rutile. The direction of the compression axis remains unknown in the images because the particles lost their original orientation after recovery. The powder was sintered with crystal sizes ranging from the sub-nano range to ~ 2 µm (Fig. 4a). In contrast to the shocked single

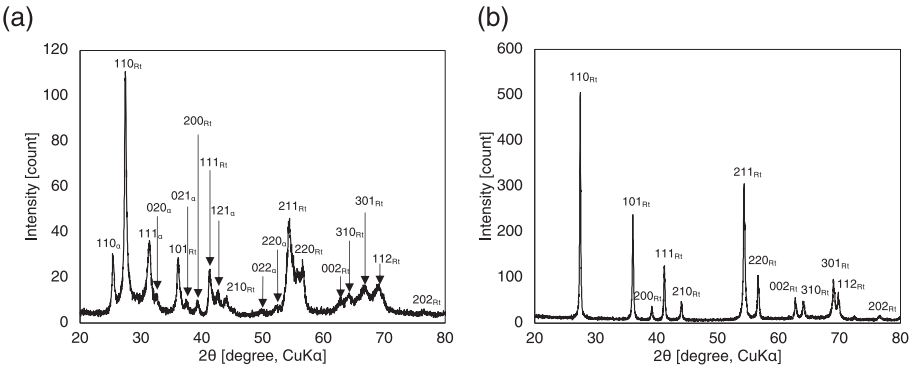

Figure 2. XRD profiles obtained from (a) the shocked single crystal rutile at 30 GPa and (b) the shocked powdered rutile at 30 GPa. Rt and α denote the rutile structure and the α-PbO_2 structure, respectively.

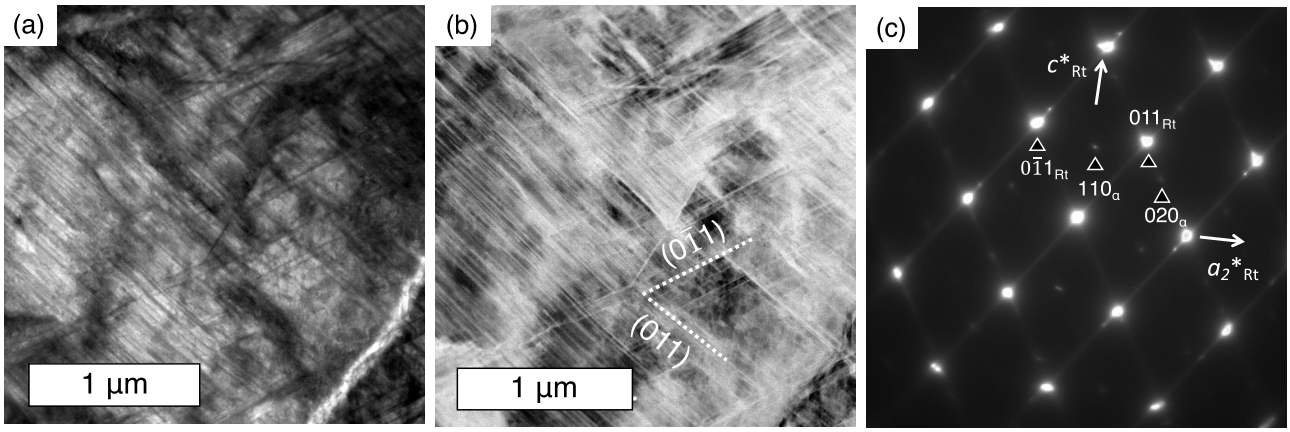

Figure 3. TEM analysis of the shocked single crystal rutile at 30 GPa. (a) BF-TEM and (b) LAADF-STEM images showing stacking faults on the {011} planes of rutile (Rt). The direction of the compression axis $[100]_{Rt}$ perpendicular to the paper surface. (c) SAED pattern of rutile along the [100] zone axis obtained from the area in the images (a) and (b). Weak diffraction patterns of the α-PbO_2 structure (α) along the [001] zone axis were also observed.

crystal, stacking faults were rarely observed in the shocked powder, whereas several particles showed pervasive entangled dislocations (Fig. 4b). The SAED patterns of the particles showed the distorted rutile diffraction spots (Fig. 4c). In contrast, some particles were nearly dislocation-free (Fig. 4d). The SAED patterns of these particles showed the sharp diffraction spots of rutile (Fig. 4e). These two particles existed in equal ratios and were spatially and randomly distributed. Only a few particles formed stacking faults (Fig. 4f). The SAED pattern of the particles confirmed the presence of $\{101\}_{Rt}$ twin lamellae (Fig. 4g). In addition, the diffraction peaks were accompanied by weak streaks along the [101]* direction, similar to the shocked single crystal.

DISCUSSION

Effect of heating on shock deformation microstructures

Shock recovery experiments conducted on the single crystal rutile and the powdered rutile showed significant differences in their microstructural features, even if they were shock-compressed at the identical peak pressure. In the shocked single crystal, stacking faults were prevailing on the $\{101\}_{Rt}$ planes throughout the thin section. In contrast, only about half of the particles of the shocked powder exhibited a high density of entangled dislocations, whereas the stacking faults were rarely observed throughout the thin section (Fig. 4a). Such stark contrast in the defect microstructures should have resulted from the different plastic deformation process under the high-stress fields during shock compression. In the powder XRD patterns, all diffraction peaks of the shocked single crystal (Fig. 2a) were broadened, indicating that large strain remained even after the complete pressure release because of complex cross-cutting between the stacking faults. Meanwhile, smaller strain in the bulk shocked powder as shown by its much sharper diffraction peaks would be caused by extensive stress relaxation due to the higher shock temperature.

A perfect dislocation is defined by the length of its

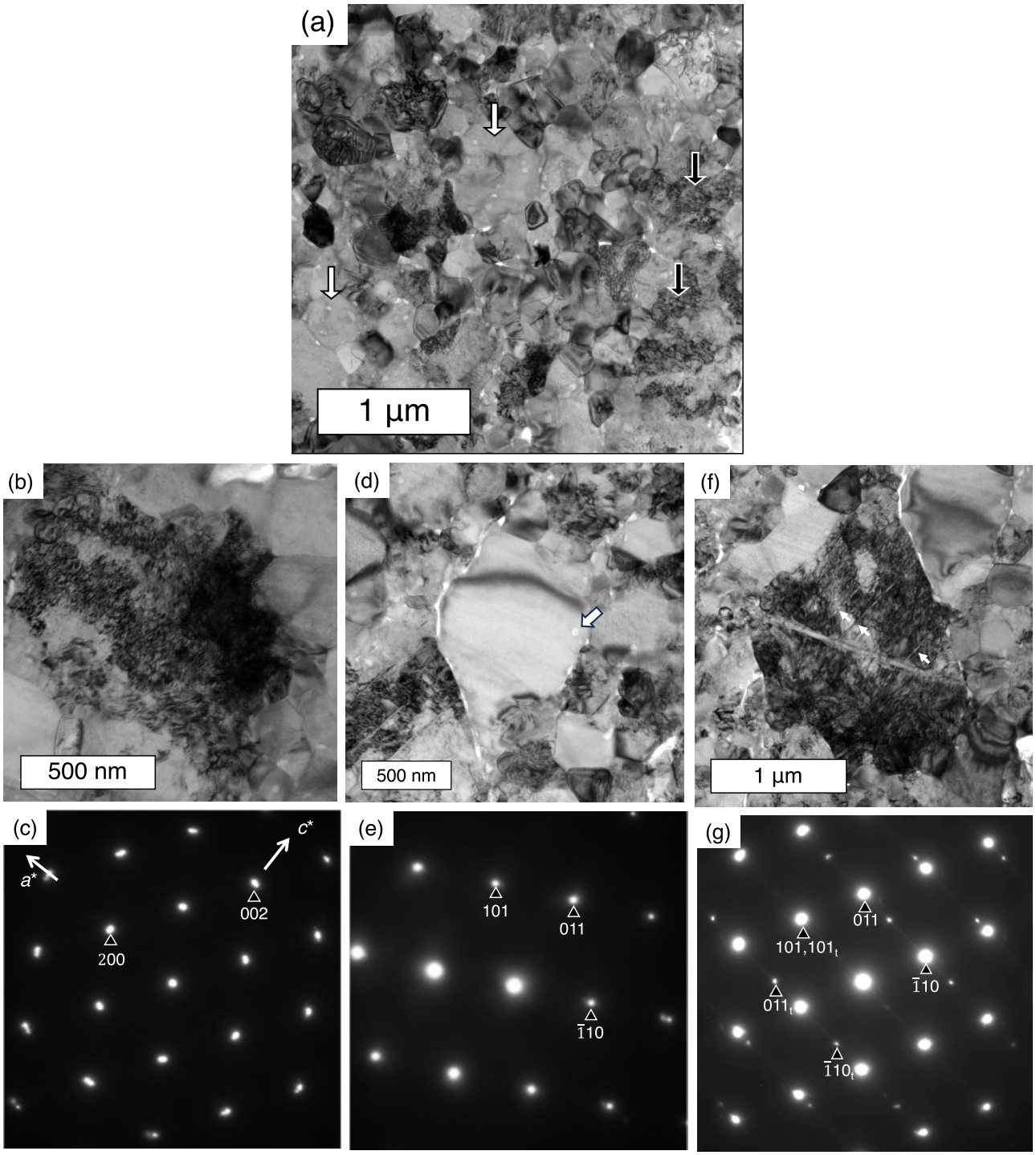

Figure 4. TEM analysis of the shocked powdered rutile at 30 GPa. The sample consisted only of rutile particles. (a) BF-TEM image showing a representative texture comprising deformed particles (indicated by black arrows) and undeformed particles (indicated by white arrows). (b) BF-TEM image of a particle with entangled dislocations. (c) SAED pattern obtained from the area in (b). (d) BF-TEM image of a particle without dislocations. The particle contained a vesicle in its rim (indicated by an arrow). (e) SAED pattern obtained from the area in (d). (f) BF-TEM image of a particle with the (101) twin lamellae (indicated by arrows). (g) SAED pattern obtained from the area in (f). t denotes twin domain.

Burgers vector, an integer multiple of the translation vector of the crystal lattice. In particular, a perfect dislocation splits into partial dislocations to optimize thermodynamic conditions. The expanded interspace between two partial dislocations yields a stacking fault (Putnis, 1992). The formation of the partial dislocations can be interpreted

in terms of the strain energy of the crystal lattice. The energy of dislocations is expressed as Kb^2, where K is the energy factor, and b is the magnitude of the Burgers vector. A perfect dislocation can be split into two partial dislocations with a stacking fault if the energy balance is

$$K_1 b_1{}^2 > K_2 b_2{}^2 + K_3 b_3{}^2$$

where subscripts 1 denotes the perfect dislocation, and 2 and 3 indicate partial dislocations.

Two principal slip systems have been reported for rutile: (i) {101}<$\bar{1}$01> and (ii) {110}<001> (Hirthe and Brittain, 1962; Ashbee and Smallman, 1963). Comparing (i) and (ii) slip systems, the perfect dislocation energies for (i) and (ii) were 0.45 (10^{-2} dyn/nm^2) and 0.17 (10^{-2} dyn/nm^2), respectively (Motohashi et al., 1979). Consequently, the dislocations in the slip system (i) are more likely to split into partial dislocations, forming stacking faults. In contrast, the slip system (ii) is energetically more favorable for forming perfect dislocations. These results are consistent with the present results, showing that stacking faults dominate on $\{101\}_{Rt}$ planes only in the single crystal rutile.

Temperature affects the activity of slip systems of rutile. Blanchin et al. (1990) suggests that the slip system (i) is predominantly active at ~ 1150 °C. It was observed that the slip system (i) was the most active direction and was able to move at a relatively lower temperature (Ashbee and Smallman, 1963). In contrast, the slip system (ii) was active at temperatures as high as ~ 1450 °C. We estimated the peak shock temperature of the single crystal rutile to be about 900 °C by evaluating the increase in the internal energy (Meyers, 1994). We can assume that the peak shock temperature of the powdered rutile surpasses this temperature value attributed to the porosity effect (Zel'Dovich and Raizer, 2002). The fully annealed particles without dislocation microstructures were identified in the shocked powdered rutile but not in the shocked single crystal rutile. Therefore, we propose that the system (i) was predominantly activated in the shocked single crystals, whereas the system (ii) was activated in the shocked powder. Our results, indicating the dominance of slip system (ii) under high-temperature conditions, are consistent with those of Blanchin et al. (1990). However, further investigation is necessary to explore the relationship between temperature and the slip system.

The activation of the slip system is also dependent on the compression direction. In our shock experiment on the single crystal rutile, the compression direction was perpendicular to the [001] direction of rutile. Therefore, the slip system (ii) was unlikely to be activated, whereas the slip system (i), as characterized by stacking faults, should have been dominant instead. Meanwhile, stacking faults were rare in the powdered rutile, although the random crystal orientation allows many of the particles to be preferentially oriented to the slip system (i). We conclude that the difference in the deformation microstructures between non-porous and porous samples is more influenced by the shock temperature than the crystal orientation.

High-pressure structural transformation of rutile through the shear mechanism

The formation of partial dislocations associated with stacking faults is essential in facilitating polymorphic structural transitions via a shear mechanism. This mechanism is expressed by the shear of the crystal lattice without atomic migration beyond the lattice dimensions. A similar mechanism has been proposed for high-pressure transformations of metals and silicates (Poirier, 1981; Bassett and Huang, 1987; Tomioka, 2007).

Both the ideal crystal structures of rutile and α-PbO_2 consist of hexagonal close-packed (hcp) oxygen anions (O'Keeffe, 1984). Meanwhile, the geometries of the titanium cation positions in these structures are different. If the rutile structure is assumed to transform directly into the α-PbO_2 structure under shock compression, the titanium cations have to move a nontrivial distance in the hcp framework of the oxygen anions within ~ 1 microsecond as time scale for the shock experiments (Kusaba et al., 1988). To reconcile the above problem, a shear transformation mechanism in the transition from rutile to the α-PbO_2 structure via the fluorite structure was originally proposed by Hyde et al. (1972). This pathway was proposed because the positions of the titanium cations in the fluorite structure are intermediate between rutile and the α-PbO_2 structure. Kusaba et al. (1988) found a topotaxial relationship between rutile and the α-PbO_2 structure in their shock-compressed samples, supporting the transformation model of Hyde et al. They proposed that rutile transformed to the fluorite structure under shock compression, and subsequently transformed to the α-PbO_2 structure under decompression. In this study, the same crystallographic relationship $<100>_{Rt}$ // $<001>_{\alpha}$ reported by Kusaba et al. (1988) was observed in the shocked single crystal rutile. We will further develop the model for the above shear mechanism by introducing stacking faults and partial dislocations.

This study presented a detailed shear deformation model of rutile forming the α-PbO_2 structure via the fluorite structure under shock compression to explain the relationship between defect structures and phase transformations. Figures 5a and 5b show one oxygen layer and

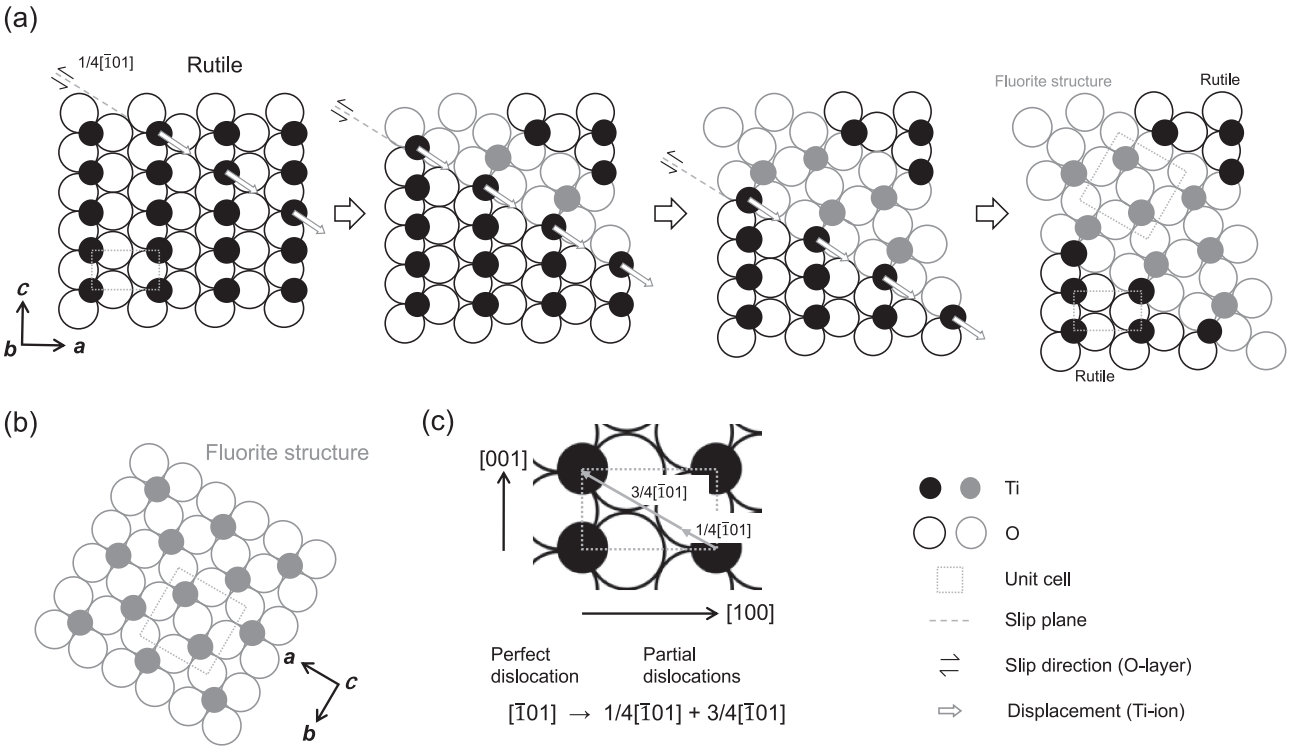

Figure 5. A model for the shear mechanism in the transition from rutile to the fluorite structure. (a) Arrangements of the titanium cations and the oxygen anions in the ideal rutile structure and their displacements during the slip of the oxygen layers along the [$\bar{1}$01] direction on the (101) plane to produce the fluorite structure. The titanium cations are displaced in the opposite direction to that of the oxygen layers. (b) Arrangements of the titanium cations and the oxygen anions in the fluorite structure. (c) Dissociation of the [$\bar{1}$01] perfect dislocation into two partial dislocations to be promoted by the slip of the oxygen layers on the (101) plane.

one titanium layer of simplified rutile and fluorite structures along the [010] and [001] directions, respectively. The rutile structure comprises a hcp of oxygen anions. Interstitial titanium cations are located at the oxygen 6-fold coordinated site (Fig. 5a). Meanwhile, the fluorite structure comprises a primitive packing of oxygen anions and interstitial titanium cations at the oxygen 8-fold coordinated site (Fig. 5b). The slip directions of the oxygen layers in Figure 5a are [$\bar{1}$01] on the (101) plane of rutile. The displacement vector of the oxygen layers is 1/4[$\bar{1}$01], which is nearly equal to the radius of the oxygen anions. The titanium cations cooperating with the oxygen layers are displaced by vector 1/4[$\bar{1}$01].

In the case of deformation in the {101}<$\bar{1}$01> slip system, the slip of the oxygen layers and the associated displacement of the titanium cations occurred randomly on the (101) plane. These ionic movements are achieved by forming partial dislocations (Fig. 5c), and the interspace between the two partials occurred as a stacking fault of the (101) plane. When the slip on the (101) plane occurs on neighboring oxygen layers, oxygen anions form primitive packing, and the titanium cations find their positions in the oxygen 8-fold coordinated site in the sheared oxygen layers. The ionic arrangement corresponds to the fluorite structure (Fig. 5b). The fluorite and the α-PbO_2 structures have a similar arrangement of titanium cations. Therefore, the fluorite structure readily transforms to the α-PbO_2 structure through the slight displacement of the oxygen layers during decompression (Kusaba et al., 1988).

This study showed that heating related to porosity significantly affects the deformation mechanism, dominant slip systems, and structural phase transitions of rutile. Because natural samples such as meteorites and crater rocks are more or less porous, the effect of shock heating must also be considered for accurate evaluation of their shock stages. Finally, these findings may contribute to the understanding of the formation histories of the Ries and the Chicxulub impact craters, where shocked titanium oxide minerals have been identified (El Goresy et al., 2001; Kring et al., 2020), although further systematic experiments are necessary to investigate the effects of porosity (i.e., shock temperature) on the mineral microstructures as pressure indicators.

CONCLUSIONS

1. Nanometer-scale microstructural observations con-

firmed the formation of stacking faults in the single crystal rutile and the formation of entangled dislocations in the powdered rutile.
2. The single crystal rutile and the powdered rutile showed the different dominant slip systems possibly affected by the different shock heating processes.
3. Porosity difference to possibly induce the different heating processes has potentially significant effects on the shock deformation microstructures and phase transition mechanisms.

ACKNOWLEDGMENTS

This study was supported by JSPS KAKENHI Grant Numbers JP22K14120 and JP21J01448 to Y.U., JP21H04519 and JP20K20947 to T.O., and JP19H05790 to H.Y. The single-stage propellant gun experiments were supported by the National Institute of Materials Science (Grant No. QN3510). This study was supported by the World Premier International Research Center Initiative (WPI). The authors thank Professors Jun Kinomura and Takaaki Noguchi at Kyoto University for their technical assistance. This study was partially supported by the Joint Usage/Research of the Institute for Integrated Radiation and Nuclear Science, Kyoto University (KURNS) (Nos. R4019, R5007, and R5073). The authors are grateful to two anonymous reviewers for their constructive reviews and comments.

REFERENCES

Ashbee, K.H.G. and Smallman, R.E. (1963) The plastic deformation of titanium dioxide single crystals. Proceedings of the Royal Society of London. Series A. Mathematical and Physical Sciences, 274, 195–205.

Bassett, W.A. and Huang, E. (1987) Mechanism of the body-centered cubic-hexagonal close-packed phase transition in iron. Science, 238, 780–783.

Blanchin, M.G., Bursill, L.A. and Lafage, C. (1990) Deformation and microstructure of rutile. Proceedings of the Royal Society of London. A. Mathematical and Physical Sciences, 429, 175–202.

Boslough, M.B. and Asay, J.R. (1993) High-Pressure Shock Compression of Solids. Springer, New York, 7–42.

El Goresy, A., Chen, M., Gillet, P., Dubrovinsky, L., et al. (2001) A natural shock-induced dense polymorph of rutile with α-PbO_2 structure in the suevite from the Ries crater in Germany. Earth and Planetary Science Letters, 192, 485–495.

Fritz, J., Greshake, A. and Fernandes, V.A. (2017) Revising the shock classification of meteorites. Meteoritics & Planetary Science, 52, 1216–1232.

Hirthe, W.M. and Brittain, J.O. (1962) Dislocations in Rutile as Revealed by the Etch-Pit Technique. Journal of the American Ceramic Society, 45, 546–554.

Hyde, B.G., Bursill, L.A., O'Keeffe, M. and Andersson, S. (1972) Continuous topological variation of coordination in crystals: Structural relations and possible transformation mechanisms. Nature Physical Science, 237, 35–38.

Kring, D.A., Tikoo, S.M., Schmieder, M., Riller, U., et al. (2020) Probing the hydrothermal system of the Chicxulub impact crater. Science Advances, 6, eaaz3053.

Kurosawa, K., Ono, H., Niihara, T., Sakaiya, T., et al. (2022) Shock recovery with decaying compressive pulses: Shock effects in calcite ($CaCO_3$) around the Hugoniot elastic limit. Journal of Geophysical Research: Planets, 127, e2021JE007133.

Kusaba, K., Kikuchi, M., Fukuoka, K. and Syono, Y. (1988) Anisotropic phase transition of rutile under shock compression. Physics and Chemistry of Minerals, 15, 238–245.

Langenhorst, F. (2002) Shock metamorphism of some minerals: Basic introduction and microstructural observations. Bulletin of the Czech Geological Survey, 77, 265–282.

Liou, J.G., Zhang, R.Y., Ernst, W.G., Rumble, D. and Maruyama, S. (1998) High-pressure minerals from deeply subducted metamorphic rocks. In Ultrahigh-pressure Mineralogy: Physics and Chemistry of the Earth's Deep Interior (Hemley, R.J. ed.). Rev. Mineralogy, 37, 33–96.

Meyers, M.A. (1994) Dynamic Behavior of Materials. pp. 668, John Wiley, New York.

Motohashi, Y., Blanchin, M.G., Vicario, E., Fontaine, G. and Otake, S. (1979) Elastic parameters, elastic energy, and stress fields of dislocations in TiO_2 rutile crystals. Physica Status Solidi (a), 54, 355–364.

Nishio-Hamane, D., Shimizu, A., Nakahira, R., Niwa, K., et al. (2010) The stability and equation of state for the cotunnite phase of TiO_2 up to 70 GPa. Physics and Chemistry of Minerals, 37, 129–136.

O'Keeffe, M. (1984) On ten- and eleven-coordinated periodic packings of equivalent spheres. Materials Research Bulletin, 19, 1433–1436.

Poirier, J.P. (1981) Martensitic olivine-spinel transformation and plasticity of the mantle transition zone. Anelasticity in the Earth, 4, 113–117.

Putnis, A. (1992) Introduction to Mineral Sciences. pp. 457, Cambridge University Press, New York.

Sekine, T. (1997) Shock wave chemical synthesis. European Journal of Solid State and Inorganic Chemistry, 34, 823–833.

Sekine, T. (2016) Experimental methods of shock wave research for solids. Hypervelocity Launchers, 55–76.

Sharp, T.G. and DeCarli, P.S. (2006) Shock effects in meteorites. Meteorites and the early solar system II, 943, 653–677.

Stöffler, D., Hamann, C. and Metzler, K. (2018) Shock metamorphism of planetary silicate rocks and sediments: Proposal for an updated classification system. Meteoritics & Planetary Science, 53, 5–49.

Syono, Y., Kusaba, K., Kikuchi, M., Fukuoka, K. and Goto, T. (1987) Shock-induced phase transitions in rutile single crystal. High-Pressure Research in Mineral Physics: A Volume in Honor of Syun-iti Akimoto, 39, 385–392.

Tan, Z., Chen, P., Zhou, Q., Liu, J., et al. (2018) Shock synthesis and characterization of titanium dioxide with α-PbO_2 structure. Journal of Physics: Condensed Matter, 30, 264006.

Tomeoka, K., Yamahana, Y. and Sekine, T. (1999) Experimental shock metamorphism of the Murchison CM carbonaceous chondrite. Geochimica et Cosmochimica Acta, 63, 3683–3703.

Tomioka, N. (2007) A model for the shear mechanism in the enstatite-akimotoite phase transition. Journal of Mineralogical

and Petrological Sciences, 102, 226–232.
Winkler, R., Luther, R., Poelchau, M.H., Wünnemann, K. and Kenkmann, T. (2018) Subsurface deformation of experimental hypervelocity impacts in quartzite and marble targets. Meteoritics & Planetary Sciences, 53, 1733–1755.
Wünnemann, K., Zhu, M. and Stöffler, D. (2016) Impacts into quartz sand: Crater formation, shock metamorphism, and ejecta distribution in laboratory experiments and numerical models. Meteoritics & Planetary Science, 51, 1762–1794.
Zel'dovich, Y.B. and Raizer, Y.P. (2002) Physics of shock waves and high-temperature hydrodynamic phenomena (Vol. 2). pp. 916, Academic Press, New York.

Manuscript received July 6, 2023
Manuscript accepted December 24, 2023
Advance online publication January 10, 2024
Released online publication February 6, 2024
Manuscript handled by Hiroaki Ohfuji